



HAL
open science

Intergranular corrosion in evolving media: Experiment and modeling by cellular automata

S. Guiso, N. Brijou-Mokrani, J. de Lamare, Dung Di Caprio, B. Gwinner, V. Lorentz, F. Miserque

► To cite this version:

S. Guiso, N. Brijou-Mokrani, J. de Lamare, Dung Di Caprio, B. Gwinner, et al.. Intergranular corrosion in evolving media: Experiment and modeling by cellular automata. Corrosion Science, 2022, 205, pp.110457. 10.1016/j.corsci.2022.110457 . hal-03725085

HAL Id: hal-03725085

<https://hal.science/hal-03725085>

Submitted on 15 Nov 2022

HAL is a multi-disciplinary open access archive for the deposit and dissemination of scientific research documents, whether they are published or not. The documents may come from teaching and research institutions in France or abroad, or from public or private research centers.

L'archive ouverte pluridisciplinaire **HAL**, est destinée au dépôt et à la diffusion de documents scientifiques de niveau recherche, publiés ou non, émanant des établissements d'enseignement et de recherche français ou étrangers, des laboratoires publics ou privés.

1 **Is there a memory effect of intergranular corrosion?**

2
3 S. Guiso^a, N. Brijou-Mokrani^a, J. de Lamare^a, D. Di Caprio^b, B. Gwinner^a, V. Lorentz^a
4 and, F. Miserque^a,
5

6 ^a Université Paris-Saclay, CEA, Service de la Corrosion et du Comportement des
7 Matériaux dans leur Environnement, 91191, Gif-sur-Yvette, France

8 ^b Chimie ParisTech, PSL Research University, CNRS, Institut de Recherche de Chimie
9 Paris (IRCP), F-75005 Paris, France
10

11 **Abstract**

12 In this paper, we investigated the impact of the oxidizing character of the nitric medium on
13 the evolution of the intergranular corrosion of a 310L austenitic stainless steel. Corroded
14 surfaces were investigated by X-ray photoelectron spectroscopy. Optical observations were
15 made to characterize the dimensions of the grooves on samples cross sections. Modeling
16 and numerical simulations were carried out by using the cellular automata method. In two
17 different stationary oxidizing conditions (“severe” in presence of oxidizing ions and “soft”
18 without, respectively), we showed that the corroded surface of the steel reaches a different
19 steady state: the oxide is thicker, the intergranular grooves are thinner and the surface area
20 is larger with the oxidizing character of the nitric medium. Then we investigated the effect
21 of an alternative “severe then soft” corrosion sequence. We showed that the system re-
22 adapted to the soft conditions without memory effect from the previous severe ones.
23

24 **Keywords**

25 Austenitic stainless steel, Cellular automata modeling, Intergranular corrosion, Nitric
26 acid, XPS

27 **Introduction**

28 Grains boundaries in materials are often considered as a weakness regarding the chemical
29 attack by the environment. The preferential attack of these grains boundaries results in a
30 specific corrosion mode named intergranular corrosion (IGC). Challenges relative to
31 intergranular corrosion concern various materials such as nickel based alloys [1-3],
32 aluminum based alloys [4-6] or steels [7-9]. One specific issue is about IGC of non-
33 sensitized stainless steels (SSs) in nitric acid. This is mainly linked to the domain of the
spent nuclear fuel reprocessing, where SSs are used for containing nitric acid solutions at

34 various concentrations and temperatures [10-12]. IGC of non-sensitized SSs is induced by
35 a differential of reactivity between grains and grains boundaries. Therefore, grain
36 boundaries are preferentially dissolved compared to the grains themselves. Consequently,
37 grooves are formed along the grains boundaries, which progression in the SS generates a
38 periodic detachment of grains.

39 Over the last fifteen years, IGC of non-sensitized SSs has been investigated through both
40 experimental and modeling approaches. From the experimental point of view, different
41 techniques are used to characterize IGC. In addition to qualitative observations of the
42 surface, optical or scanning electron microscopy can be performed on the cross section of
43 the sample to geometrically characterize the intergranular grooves in 2D [13-23]. A
44 promising 3D characterization approach has also been attempted by μ -Xray-tomography
45 [24]. The measurement of the mass loss as the function of time gives also important
46 information regarding the kinetics of IGC [13, 15, 19-21, 25-32]. Sometimes, the chemical
47 characteristics of the surface are analyzed by X-ray photoelectron spectroscopy (XPS) [15,
48 28, 33, 34]. An attempt to characterize IGC with ultrasonic methods was proposed by
49 Jothilakshmi *et al.* [22]. In addition to this experimental information, different models were
50 recently proposed to simulate IGC of non-sensitized SSs in nitric acid. A simple analytical
51 approach was proposed for simulating the evolution of the mass loss [35]. A geometrical
52 approach in 2D was developed for simulating the evolution of the interface of the material
53 suffering IGC [21, 35]. More realistic models were also developed using the method of
54 cellular automata (CA) for simulating the geometrical evolution of the material in a 3D
55 realistic granular structure [18, 32, 36-38].

56 All these experimental and modeling approaches allowed studying the influence of
57 different metallurgical and chemical parameters on IGC. It appears that IGC could be
58 dependent on the surface exposed to corrosive medium regarding the rolling direction [19,
59 20, 29, 39], on the chemical composition of the SSs, which in turn influence the chemical
60 composition of the grains boundaries [13, 14, 18, 20, 28, 31, 33, 34, 40, 41], on the grains
61 size [30] and on the metallurgical treatment [25]. IGC of SSs was also studied in a pure
62 nitric medium at different concentrations [28, 33] but also with the addition of different
63 oxidizing species at different levels [26, 27, 39, 41]. However, these parameters were only
64 correlated to the corrosion potential and corrosion kinetics, with no information on the
65 characteristics of the interface in terms of chemical composition and morphology. In this
66 paper, we intend to fill this gap by investigating IGC of a SS in two different nitric acid

67 media. We investigated the influence of the chemical medium nature on the elemental
68 composition of the oxide layer (analyzed by XPS) and the geometrical characteristics of
69 the interface. For this last one, as it was difficult to extract information from experiments,
70 we used CA modeling. Indeed, we showed that CA is able to reproduce accurately the
71 experimental behavior [23, 38].

72 Moreover, we also investigated cases where the corrosive environment evolves over time
73 during a given experiment. The objective was to study how the IGC of a given SS sample
74 may be influenced by the fact that this SS was previously corroded in a first medium. To
75 our knowledge, this aspect has never been studied despite it may concern many industrial
76 issues, for example: the case of equipments whose corrosive environment evolves with
77 time or the case of the alternation of phases of rinsing (with one first chemical medium)
78 and working (in a second chemical medium).

79

80 **Experimental and modeling approaches**

81 Experimental conditions and characterization methods

82 We performed corrosion tests (electrochemical measurements and immersion tests)
83 with an AISI 310L SS provided by Creusot Loire Industrie. This stainless steel has a low
84 carbon content and was annealed and quenched. The chemical composition is given in
85 Table 1. The mean grain size (84 μm) was determined using the normalized NF EN ISO
86 643:2003.

87

Table 1. Chemical Composition of AISI 310L SS (in wt.%).

Fe	C	Cr	Ni	Mn	Si	P	S	Mo	Nb
bal.	0.006	24.32	21.13	1.03	0.13	0.016	0.001	0.08	0.115

88

89 For the corrosion tests, the corrosion medium was 8 mol.l⁻¹ nitric acid at boiling point
90 temperature (111 °C) containing or not 150/300 mg/L of vanadium(V) (introduced as 268/
91 536 mg/L of V₂O₅). By introducing or not vanadium(V), we intended to impose different
92 oxidizing conditions to the material regarding the difference of standard potential in nitric
93 acid ($E^\circ(\text{NO}_3^-/\text{HNO}_2) = 0.934 \text{ mV/SHE}$ at 25 °C [42]) and in presence of vanadium(V),
94 ($E^\circ(\text{VO}_2^+/\text{VO}^{2+}) = 1.004 \text{ V/SHE}$ at 25 °C [42]). For the rest of the paper, we name “soft”
95 conditions” the experiments without vanadium(V) and “severe conditions” the ones with
96 additions of vanadium(V).

97

98 We performed electrochemical measurements (open circuit potential and linear
99 voltammetry measurements) using a classical 3-electrodes configuration. The working and
100 the counter electrodes were a 310L bullet shaped electrode (surface area 2 mm²) and a
101 platinum basket, respectively. The reference electrode was a mercury/mercurous sulfate
102 electrode (Hg/Hg₂SO₄ - MSE, E = +0.65 V/SHE at 25 °C). The electrochemical
103 measurements were performed using a VSP workstation controlled by the software EC-
104 Lab v.10.37 (Biologic).

105

106 The conditions and durations of the 3 immersion tests are given in Table 2. SS specimens
107 were 30 × 20 × 1.5 mm³ parallelepiped samples. They were ultrasonic degreased with an
108 ethanol/acetone mixture. They were pickled with an H₂O/HCl/HNO₃/HF mixture for
109 around 15 minutes in order to dissolve a thickness of about 20 μm. The experimental device
110 consists of a 1 L glass reactor where 3 specimens are suspended to test the reproducibility
111 of the corrosion process (the metallic surface area on the solution volume S/V ratio was
112 0.4 dm²/L). The specimens were periodically removed from the reactor, rinsed with
113 demineralized water and ethanol, dried with compressed air and weighted (AT 20 balance
114 model from Mettler-Toledo, precision 0.01 mg). The solution was renewed after each
115 corrosion period. The mass loss as a function of time was expressed in terms of equivalent
116 thickness loss assuming a hypothetical homogeneous corrosion, as follows:

$$\Delta e = \Delta m / (\rho \times S) \times 10^4 \quad \text{Equation 1}$$

117 With Δe the equivalent thickness loss (in μm)

118 Δm the measured mean mass loss (in g)

119 ρ the SS density (8 g/cm³ approx.).

120 S the sample surface (13.5 cm²)

121 Periodically, one of the samples was cut and the cross-section of the sample was optically
122 observed (GX51 microscope model from Olympus).

123

124 Table 2: Conditions of the immersion corrosion tests. In tests n°1 and n°2, the corrosive
 125 medium remained constant during the test. In test n°3, the corrosive medium was modified
 126 after 1935 h.

Test		Conditions	Duration
Test n°1		Severe	$t_{\text{severe}} = 2564 \text{ h}$
Test n°2		Soft	$t_{\text{soft}} = 16815 \text{ h}$
Test n°3	Phase n°1	Severe	$t_{\text{severe}} = 1935 \text{ h}$
	Phase n°2	Soft	$t_{\text{soft}} = 16815 \text{ h}$ $(t_{\text{test3}} = t_{\text{severe+soft}} = 17783 \text{ h})$

127

128 XPS analyses were carried out with a Thermofisher Escalab 250 XI spectrometer using
 129 a monochromatic X-ray Al Ka source. The instrument was calibrated in energy with the
 130 Ag Fermi level (0 eV) and the 3d_{5/2} core level of metallic silver (368.3 eV). The C-1s signal
 131 was used to correct a possible charge effect: the CC/CH contribution of C-1s spectra was
 132 fixed at 285.0 eV. The analysis zone consisted of a 900 μm diameter spot. The data
 133 processing was performed using the commercially available Avantage™ software. For the
 134 fitting procedure, a Shirley background has been used and Lorentzian-Gaussian (L/G) ratio
 135 was fixed at 30%. For the determination of relative proportions of oxide and metallic
 136 contribution, Ni-2p_{3/2}, Cr-2p_{3/2} and Fe-2p_{3/2} spectra have been deconvoluted. The main
 137 contributions used are presented in Table 3. Several arbitrary contributions are necessary
 138 to fit the iron and chromium oxide due to a multiplet splitting making the spectral analysis
 139 particularly complex [43, 44]. Nickel element is observed only metallic chemical state.

140

141 Table 3: Parameters used for the deconvolution of Cr, Ni and Fe-2p_{3/2} core level spectra
 142 (Avantage™ software) binding energies and full width at half maximum (FWHM).

	Ni-2p _{3/2}	Fe-2p _{3/2}		Cr-2p _{3/2}				
Chemical state	Metallic	Metallic	Oxide		Metallic	Oxide		
			Peak 1	Peak 2		Peak 1	Peak 2	Peak 3
Binding Energy (eV)	853.0 ± 0.3	853.0 ± 0.3	709.8 ± 0.3	712.0 ± 0.3	853.0 ± 0.3	576.1 ± 0.3	577.3 ± 0.3	578.5 ± 0.3
FWHM (eV)	1.4	1.0	3.0	3.3	1.5	1.7	1.8	1.9

143

144 Cellular Automata model

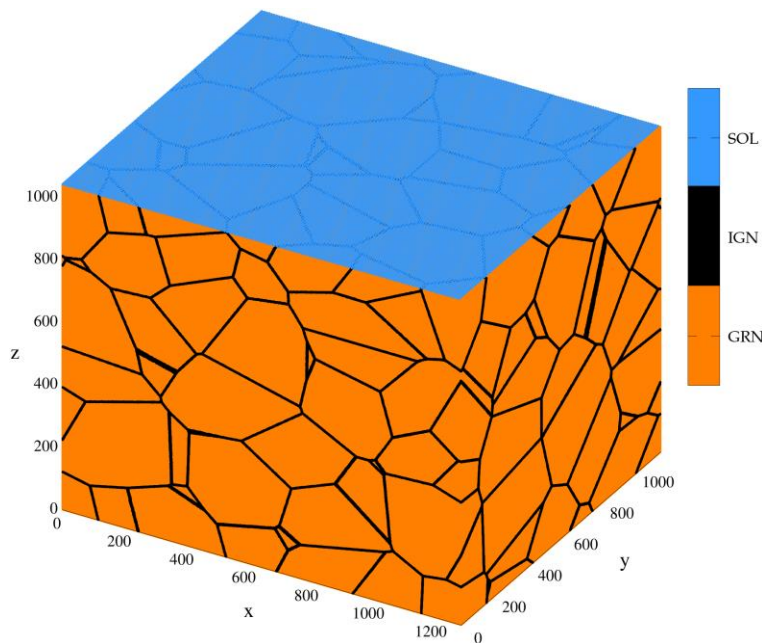
145 CA approach consists first in discretizing a volume (box) into a 3D hexagonal grid of
 146 cells. In our model ([23]), a cell can belong to a grain (GRN state), a grain boundary (IGN
 147 state) or the solution (SOL state). The material granular microstructure is obtained
 148 numerically by a Voronoi diagram (Figure 1). Furthermore, the SOL state is assigned to
 149 the three uppermost xy-layers: during dissolution, the solution path is conducted from the
 150 top of the grid to the bottom.

151 The kinetics of the reactions are hereby converted into corrosion probabilities, which
 152 drive the step from a time t to the following t + Δt. Given CA cells interact with their
 153 neighbouring ones according to their states, following transition rules. IGN and GRN cells
 154 change their states to SOL (this switch indicates that the IGN or GRN cell is corroded)
 155 according to two probabilities (input data fixed by the user), P_{ign} for grain boundaries and
 156 P_{gm} for grains. The way to fix the values of P_{ign} and P_{gm} so as to reproduce adequately the
 157 experimental results (with CA to experiments conversion factors) is described in reference
 158 [23].

159 The code has been written in C language, in CUDA environment, and numerical
 160 simulations have been performed using NVIDIA Tesla K80 in Dell PowerEdge C4130
 161 servers with Intel Xeon E5-2640 processors. In the case of a (XYZ dimensions) 3D grid, a
 162 simulation run for a single experiment takes from one to a few days, depending on the
 163 values that are given to P_{gm} and P_{ign} (the higher the values, the lower the simulation time).
 164 The grids taken for the simulation are boxes of 1280x1280x1280 cells, and the number of

165 Voronoï structures are one hundred. This corresponds to a surface dimension of 13.5 mm^2
166 and a depth of $395 \text{ }\mu\text{m}$, using the scale transformation of $0.309 \text{ }\mu\text{m}/\text{cell}$ as described in [23].
167 The results are averaged over the hundred different Voronoï structures and the errors bars
168 given further in the paper represent their dispersion.

169 From the corroded sample at a time t , we can estimate the mass loss and the mean
170 groove angle α' ([23]), as well as the relative surface in contact with the corrosive medium
171 (see appendix 1 and 2). Note that the notation α' refers to the angle determined in 2D from
172 virtual cross-sections of the 3D grid and that its distribution is slightly different from the
173 3D angles α distribution as discussed in [23, 24].
174



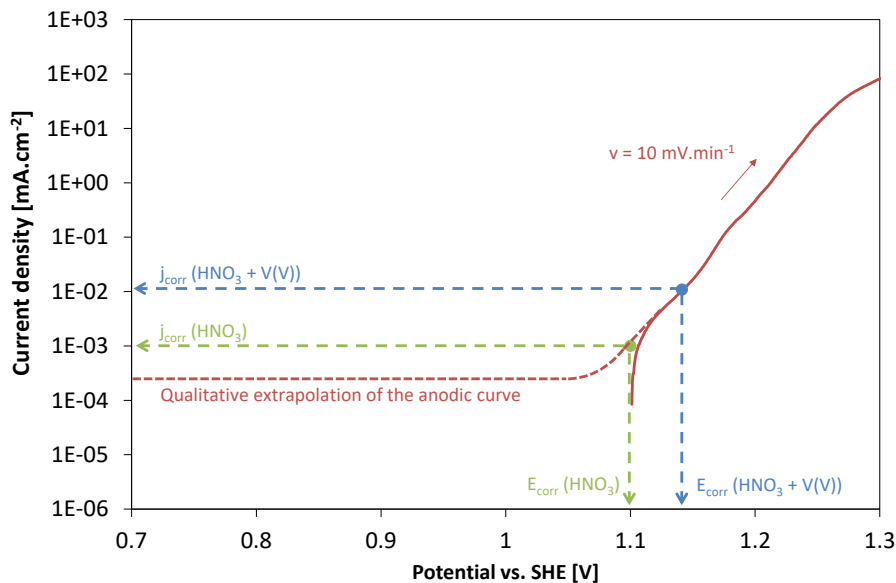
175 **Figure 1: Representation of a 3D initial grid considered for the IGC model obtained**
176 **numerically by a Voronoï diagram (GRN state cell in orange, IGN state cell in black**
177 **and SOL state cell in blue).**
178
179

180 Results

181 Electrochemical measurements

182 We performed preliminary electrochemical measurements in order to specify the
183 conditions of corrosion in both configurations “severe” and “soft”. Figure 2 presents the
184 anodic linear polarization of the 310L SS in nitric acid HNO_3 8 mol.l^{-1} at boiling point
185 temperature. Based on the results obtained for a similar system [15], we qualitatively
186 extrapolated the anodic curve below the corrosion potential E_{corr} (that is not directly
187 measurable by electrochemistry because of the cathodic reactions) in order to visualize the

188 respective position of the passive and transpassive domain of the SS. Thus, we observe that
 189 in these conditions, the SS is polarized ($E_{\text{corr}} \sim 1.11 \text{ V vs. SHE}$) in the transition of the
 190 passive to transpassive domains, where IGC is expected. In addition to vanadium(V), E_{corr}
 191 is shifted to a higher anodic potential ($E_{\text{corr}} \sim 1.14 \text{ V vs. SHE}$) in the transpassive domain,
 192 where IGC is also expected. The expected corrosion currents are given in Figure 2, which
 193 shows that a higher corrosion rate is expected in presence of vanadium(V).
 194 In conclusion, SS is polarized in both conditions in the transpassive domain, where IGC is
 195 expected. The objective of the following parts is to characterize IGC in both conditions.



196
 197 **Figure 2: Anodic linear polarization curve of 310L SS in HNO_3 8 mol.l⁻¹ at boiling**
 198 **point temperature (red continuous line). The red dashed line represents the**
 199 **qualitative extrapolation of the anodic curve in the passive domain. The**
 200 **characteristics (E_{corr} and j_{corr}) of the system are in green. Those of the system Uranus**
 201 **65 in HNO_3 8 mol.l⁻¹ + V(V) 150 mg.l⁻¹ are in blue.**

202
 203 Immersion tests

204 In this part, we discuss the case IGC in both oxidative conditions, respectively, when the
 205 chemical medium remains the same as a function of time. The corrosion kinetics is given
 206 in terms of morphology (Figure 3 (a) for severe and Figure 5 (a) for soft conditions) and
 207 mass loss (expressed in terms of equivalent thickness loss as described in the experimental
 208 section) and corrosion rate (Figure 4 for severe and Figure 6 for soft conditions). The
 209 behavior is typical of the IGC observed for non-sensitized stainless steels and has been
 210 extensively discussed in references [15, 21, 35].

211 IGC begins with the creation of tight grooves at grains boundaries (80 h and 240 h in Figure
 212 3 (a)) that progressively penetrate the steel. This leads to an increase of the SS/solution
 213 interface area, which is correlated to the corrosion rate increase as estimated by mass loss
 214 (Figure 4). This also leads to the detachment of grains that progressively affect the whole
 215 surface (2484 h in Figure 3 (a)) increasing the corrosion rate even more. When the grains
 216 detachment has affected the whole surface, the system reaches a corrosion steady state. The
 217 surface area does not evolve anymore, since the progression of grooves (increasing
 218 interface area) is counter-balanced by the grains detachment (decreasing the interface area).
 219 The phenomenology is similar for both oxidizing conditions, but the kinetics is different.
 220 It has been shown that this kind of IGC can be described by two different corrosion rates:
 221 V_{grn} and V_{ign} which correspond to corrosion rates of the grains and grains boundaries
 222 respectively. From the kinetics of IGC (Figure 4 and Figure 6), it is possible to estimate
 223 the values of V_{grn} and V_{ign}^* (corresponding to the projection of V_{ign} on the vertical axis) by
 224 a semi-empirical approach presented in [35]. V_{ign} is deduced from V_{ign}^* using a tortuosity
 225 factor k : $V_{ign} = V_{ign}^* \times k$, with $k = 1.18$ [23]. Results are given in Table 4. Both corrosion
 226 rates are faster in severe than in soft conditions. This confirms the forecasting from the
 227 electrochemical results (Figure 2).

228 The transient time necessary to reach the steady state can be estimated as follows [35]:

$$\frac{3}{2} \frac{D}{V_{ign}} \quad \text{Equation 2}$$

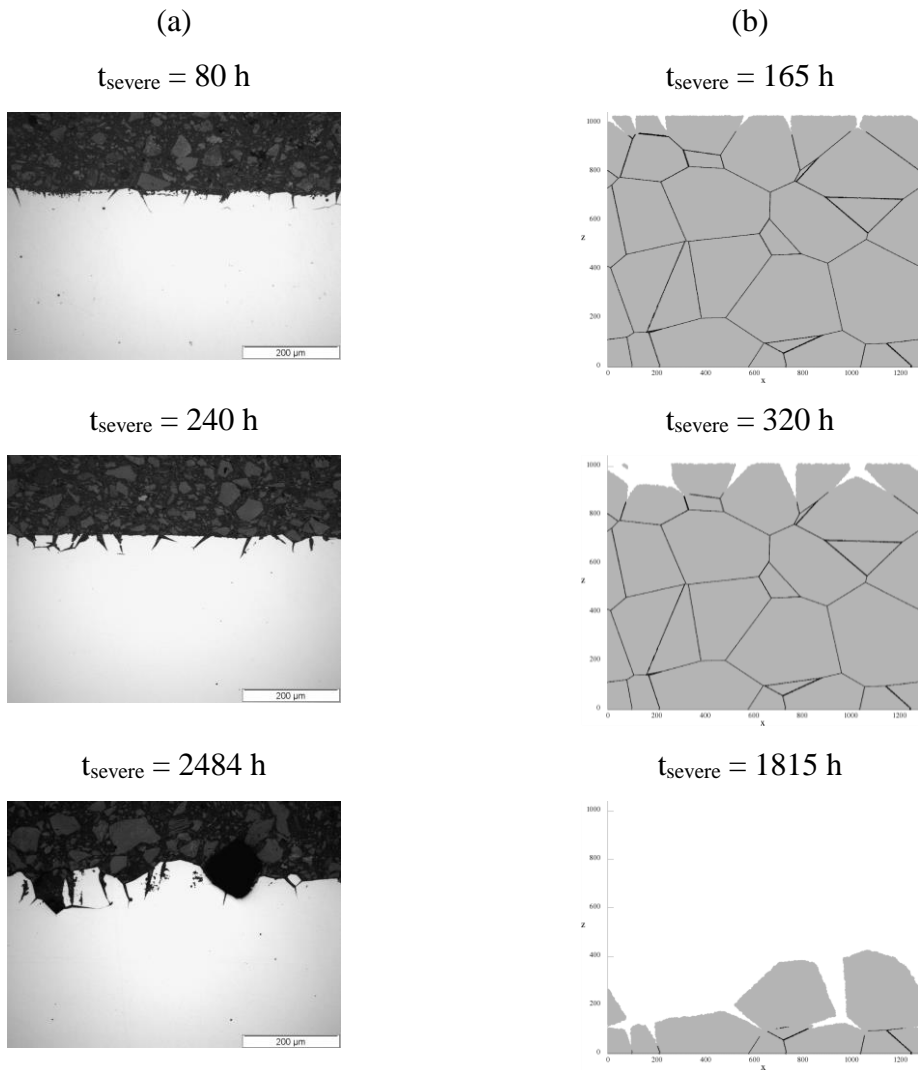
229 where D represents the average grains diameter ($84 \mu\text{m}$). Therefore, the transient time is
 230 lower in severe conditions (Table 4). Durations of the experiments were fixed so that the
 231 steady state could be almost reached in both cases, that is 2564 h for severe and 16815 h
 232 for soft conditions, respectively. The objective of the following characterizations is to
 233 investigate the surface properties at steady state.

234

235 Table 4. Corrosion rates and transient time for the severe and soft IGC cases

IGC	$V_{grn} / \mu\text{m.y}^{-1}$	$V_{ign}^* / \mu\text{m.y}^{-1}$	$V_{ign} / \mu\text{m.y}^{-1}$	Transient time / h
severe	273	1656	1954	565
soft	12	56	66	16703

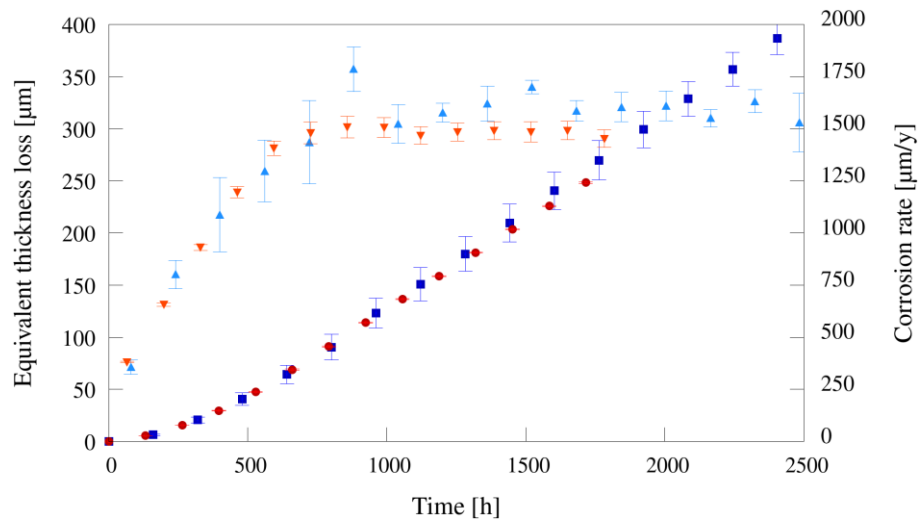
236



237 **Figure 3: Evolution of the IGC observed on cross-sections in the case of a severe IGC.**

238 **(a) Experiment (b) CA simulations at different times.**

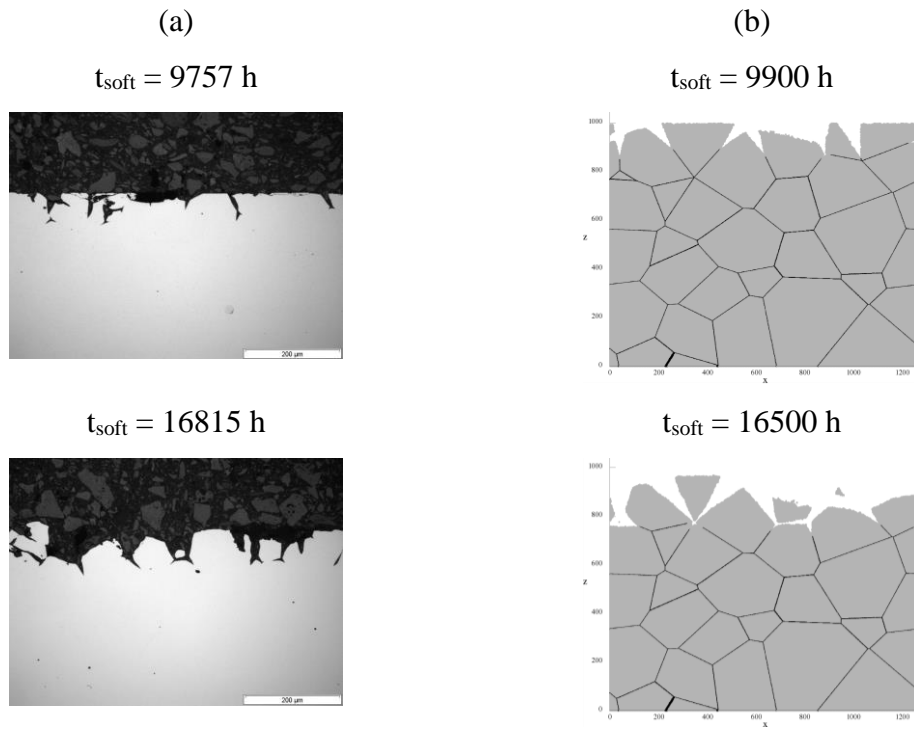
239



240

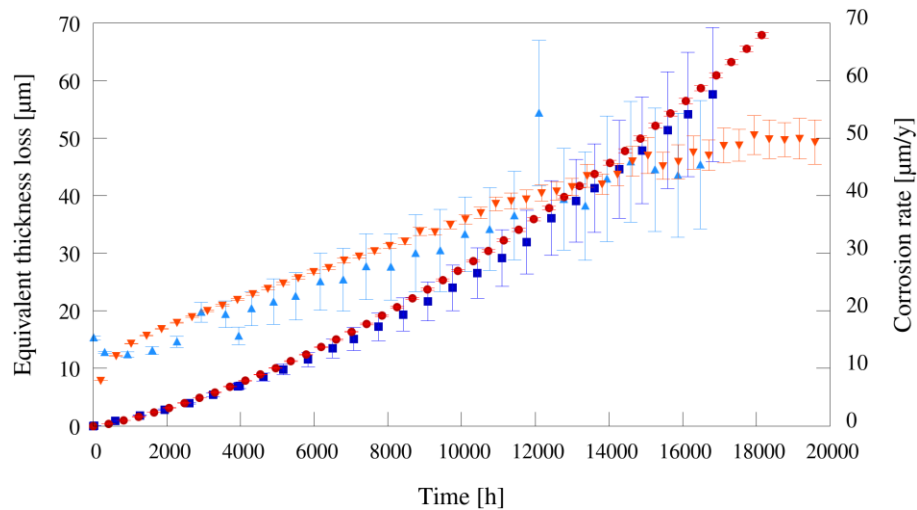
241 **Figure 4: Comparison between experimental results (in blue) and CA simulations (in**
 242 **red) in the case of a severe IGC. Squares represent the equivalent thickness loss and**
 243 **triangles the corrosion rate.**

244



245 **Figure 5: Evolution of the IGC observed on cross-sections in the case of a soft IGC.**
 246 **(a) Experiment (b) CA simulations at different times.**

247



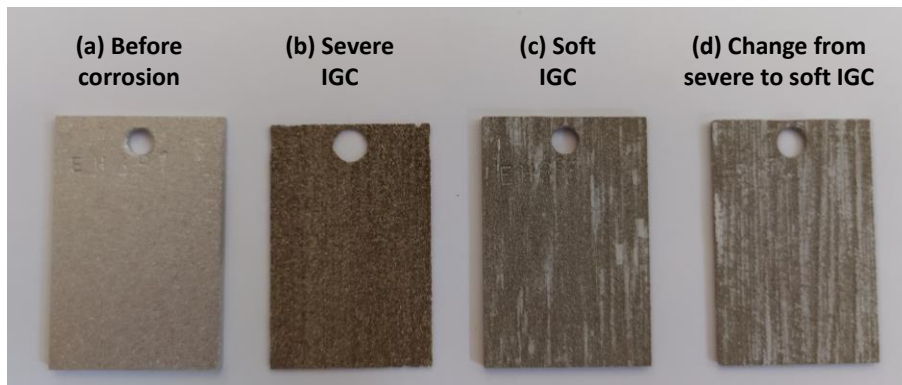
248

249 **Figure 6: Comparison between experimental results (in blue) and CA simulations (in**
 250 **red) in the case of a soft IGC. Squares represent the equivalent thickness loss and**
 251 **triangles the corrosion rate.**

252

253 Figure 7 presents the observation of the samples before (a) and after the corrosion tests in
 254 severe (b) and soft (c) conditions. In both conditions, samples are darker after corrosion
 255 then indicating an effect of the corrosion on the surface. Moreover, the aspect of samples
 256 is different between the severe (dark grey) and the soft (light grey). This shows that the
 257 aspect of the corroded SS is also dependent on the conditions of corrosion. The origin of
 258 the difference of aspect is further discussed in terms of chemical composition and IGC
 259 morphology of the interface.

260



261

262 **Figure 7: Aspect of the samples before (a) and after the corrosion tests in the severe**
 263 **($t_{\text{severe}} = 2564$ h) (b), soft ($t_{\text{soft}} = 16815$ h) (c) and change from severe ($t_{\text{severe}} = 1935$ h)**
 264 **to soft ($t_{\text{soft}} = 16815$ h, *i.e.* $t_{\text{severe+soft}} = 17783$ h) conditions (d).**

265

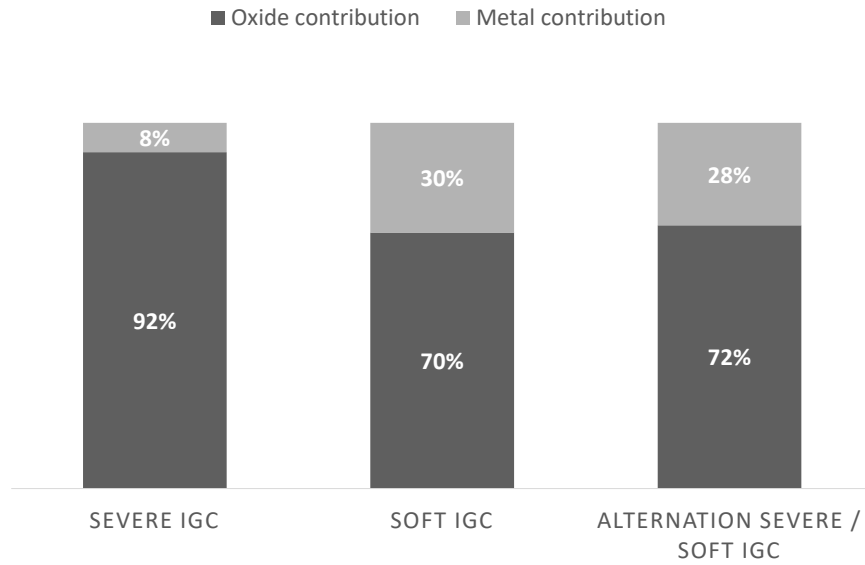
266 Therefore, we analyzed the chemical composition of the surface using XPS relative
267 quantification in both conditions (Figure 8). The XPS response is qualitatively similar in
268 severe and soft conditions. The spectra show the presence of oxide and metal (associated
269 to the presence of the metal under the oxide layer). The relative proportions of the oxide
270 and metal contributions (for the major elements contained in the 310L SS: Iron, nickel,
271 chromium) are reported in Figure 8 (a). The relative contribution of the oxide is larger in
272 the severe than in the soft IGC conditions. This indicates that the oxide layer is thicker in
273 the severe IGC conditions (with a higher corrosion potential E_{corr} as illustrated in Figure 2)
274 than in the soft IGC conditions. This is in accordance with the results of Tcharkhtchi *et al.*
275 who showed an increase of the oxide thickness of a 304L SS in nitric acid with the increase
276 of the corrosion potential E_{corr} [15].

277 Figure 8 (b) gives the chemical composition of the oxide layer. As classically observed for
278 these SSs corroded in nitric acid media [15, 34, 45], the oxide is mainly composed of
279 chromium with a small proportion of iron. Nickel oxide is not observed. The severe/soft
280 IGC conditions have a small influence on the chromium/iron ratio: a little larger relative
281 enrichment in chromium is observed for the severe condition.

282 The chemical composition of the underlying metal is given in Figure 8 (c). Its relative
283 composition differs from the bulk material: relatively enriched in nickel, compared to
284 chromium and iron. This observation has already been reported for SSs in nitric acid [15].
285 It could be due to the fact that nickel is less oxidized than chromium and iron (as illustrated
286 in Figure 8 (b)) and consequently accumulates under the oxide. This nickel enrichment
287 seems to be larger in the severe conditions than in the soft conditions. This could be linked
288 to the fact that the metallic zone that is analyzed by XPS is thicker (because the oxide is
289 thinner) in soft conditions than in severe conditions. Therefore, the nickel relative
290 enrichment in the underlying metal is more averaged with the bulk metal composition in
291 the soft than in the severe conditions.

292

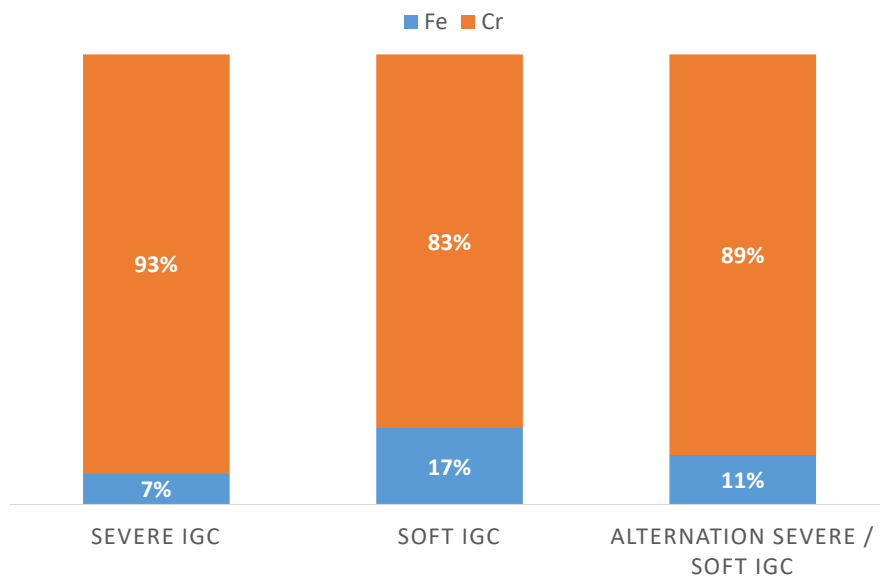
293 (a) Relative quantification of the total oxide and the underlying metal contributions (for
294 the major elements contained in the 310L SS: Fe, Ni, Cr)



295

296

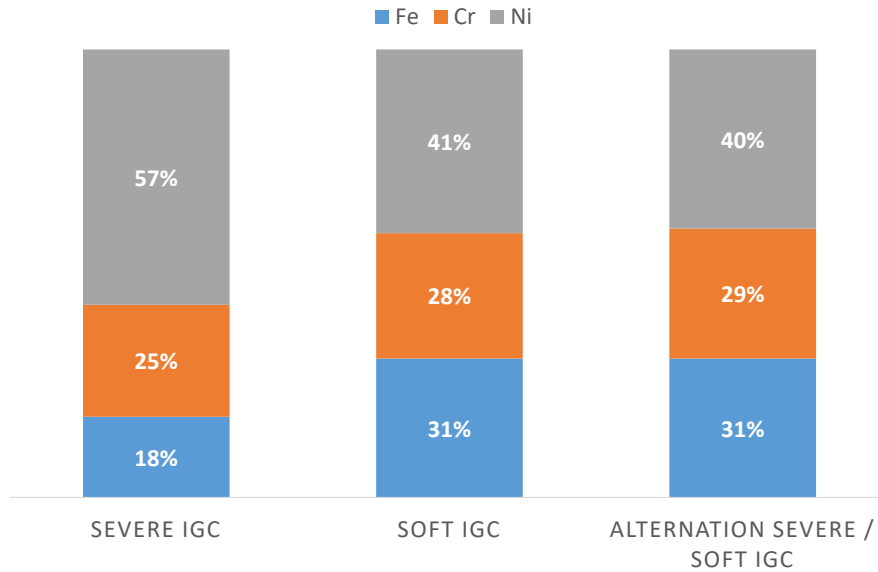
(b) Relative quantification of the composition of the oxide layer



297

298

(c) Relative quantification of the composition of the underlying metal



299

300 **Figure 8: XPS relative quantification of the chemical characteristics of the surface of**
 301 **310L SS samples corroded in the severe ($t_{\text{severe}} = 2564$ h), soft ($t_{\text{soft}} = 16815$ h) and**
 302 **change from severe ($t_{\text{severe}} = 1935$ h) to soft ($t_{\text{soft}} = 16815$ h, i.e. $t_{\text{severe+soft}} = 17783$ h)**
 303 **conditions.**

304

305 In order to get a quantitative description of the morphology, we used a CA modeling of the
 306 experiments. In a previous work [23], we showed that this model reproduces accurately the
 307 morphological evolution of IGC. This CA numerical approach enables to quantify
 308 precisely the morphological characteristics of the system, in terms of grooves angles α'
 309 distribution and the surface in contact with the solution.

310 The input corrosion probabilities are given in Table 5 for both IGC conditions. Moreover,
 311 conversion factors were also used in order to convert space and time scales from CA
 312 modeling to real experiments [23]: the space scaling factor A and time the scaling factor B
 313 were fixed to $0.31 \mu\text{m}/\text{cell}$ and $0.825 \text{ h}/\text{iteration}$, respectively. CA simulated time
 314 evolutions of the mass loss (as expressed in terms of equivalent thickness loss) are given
 315 in Figure 4 and Figure 6.

316 The distribution of the grooves angle α' (in degrees) at steady state of IGC is given in
 317 Figure 9. It appears that the grooves are thinner in severe (mean value 20.5, standard
 318 deviation 5.0) than in soft (mean value 26.59, standard deviation 5.9) conditions. From
 319 Beaunier [46, 47], the groove angle α is theoretically related to the $V_{\text{ign}}/V_{\text{grn}}$ ratio by the
 320 relation:

$$\frac{V_{ign}}{V_{grn}} = \frac{1}{\sin(\alpha/2)} \quad \text{Equation 3}$$

321

322 This theoretical value is in agreement with the one estimated by CA.

323 In conclusion, it appears that the more oxidant the corrosive solution, the thinner the
324 grooves and the larger the ratio V_{ign}/V_{grn} .

325 SEM images of the corroded samples are given in Figure 10. It is clearly visible that there
326 are less “small grains” that remain attached to the bulk in the severe case (a) than in soft
327 case (b). It is due to a larger V_{ign}/V_{grn} in case (a) (Table 4), which leads to a larger grains
328 detachment rate. From the time they are in contact with the corrosive solution, small grains
329 are more rapidly detached from the bulk than large ones, which explains the lack of small
330 grains on a given surface picture in the case of severe corrosion, given their shorter “life-
331 time”. As another effect of the grains life-time, it is also clearly visible in (b) and (c) that
332 large grains that remain attached to the bulk are more deeply corroded than the small ones.

333

334 Table 5: Corrosion probabilities used as input data in the CA model and calculated from
335 the experimental results based on the procedure given in reference [23].

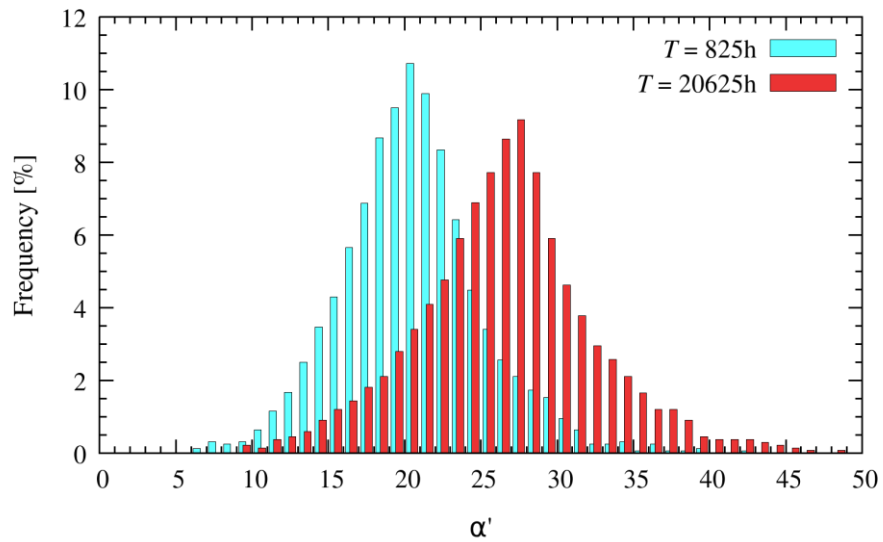
	P_{ign}	P_{grn}
Severe	$P_{ign,severe} = 1$ (arbitrary maximized in order to minimize the calculation durations)	$P_{grn,severe} = P_{ign,severe} \times \frac{V_{grn,severe}}{V_{ign,severe}}$ $P_{ign,soft} = 0.140$
Soft	$P_{ign,soft} = P_{ign,severe} \times \frac{V_{ign,soft}}{V_{ign,severe}}$ $P_{ign,soft} = 0.0338$	$P_{grn,soft} = P_{ign,soft} \times \frac{V_{grn,soft}}{V_{ign,soft}}$ $P_{grn,soft} = 0.00614$

336

337 Table 6: Intergranular grooves angles α' characteristics at steady state in the different
 338 corrosion conditions (CA simulations)

Exp., time	Mean value (degrees)	Standard deviation (degrees)	Error	$1/(\sin(\alpha'/2))$
Severe condition $t_{\text{severe}} = 825 \text{ h}$	20.54	5.00	0.13	5.61
Soft condition $t_{\text{soft}} = 20\ 625 \text{ h}$	26.59	5.89	0.16	4.35
Change severe $t_{\text{severe}} = 825 \text{ h}$ to soft condition	20.67	4.88	0.14	5.57
$t_{\text{severe+soft}} = 20\ 625 \text{ h}$	26.04	5.92	0.17	4.44

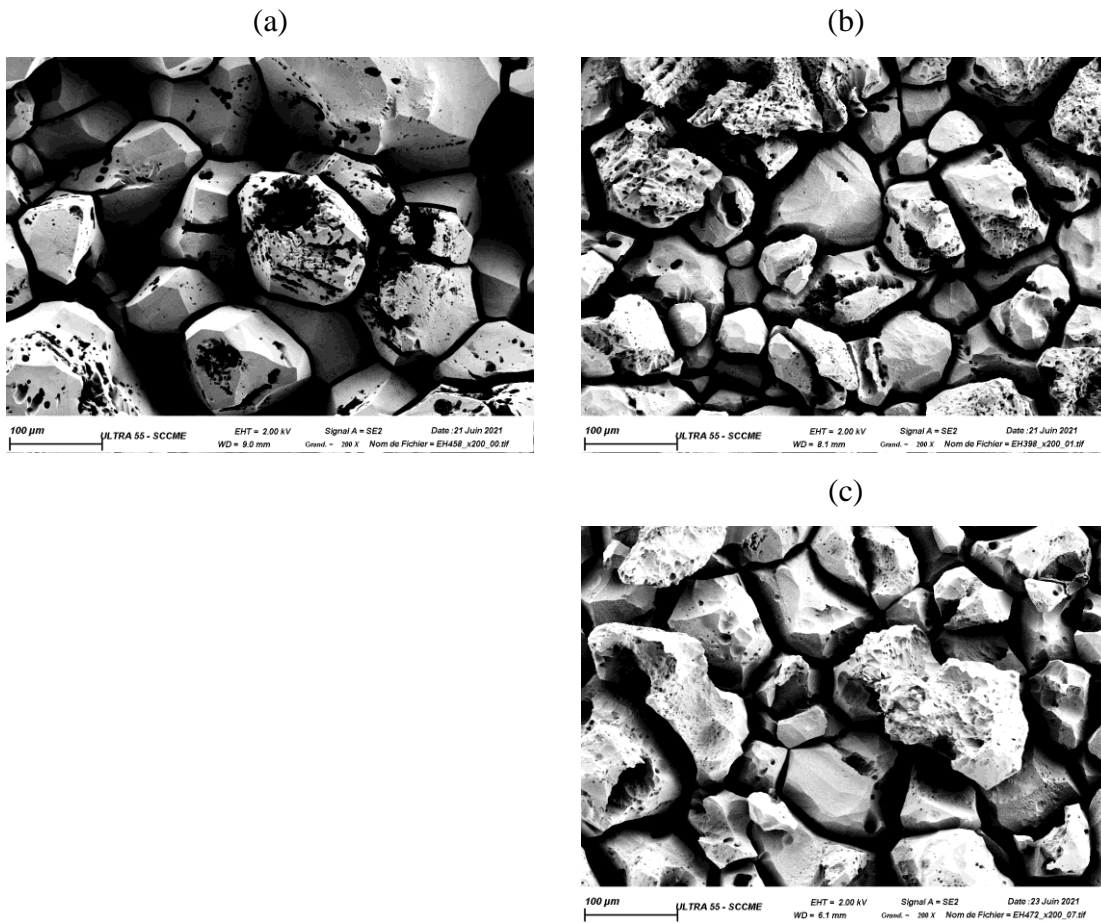
339



340

341 **Figure 9: Distribution of the grooves angles α' in the steady state in severe (in blue,**
 342 **evaluated at $t_{\text{severe}} = 825 \text{ h}$) and in soft (in red, evaluated at $t_{\text{soft}} = 20625 \text{ h}$) conditions**
 343 **(CA simulations). In both cases, histograms are realized with the same classes but are**
 344 **slightly shifted for a better view.**

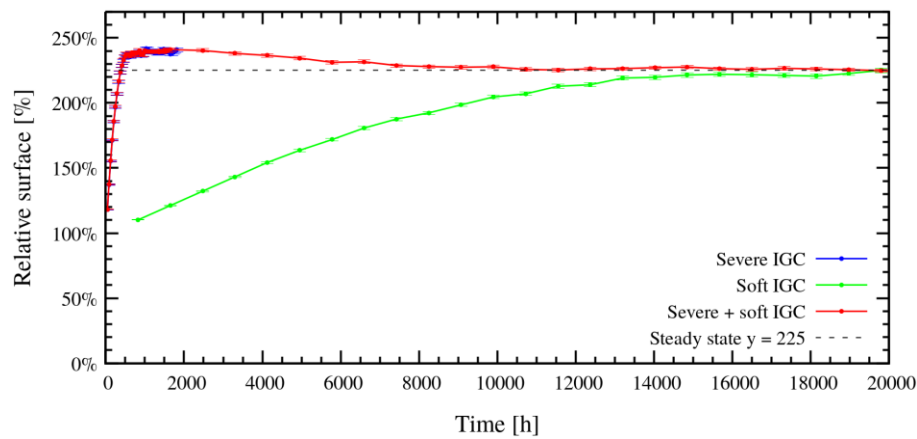
345



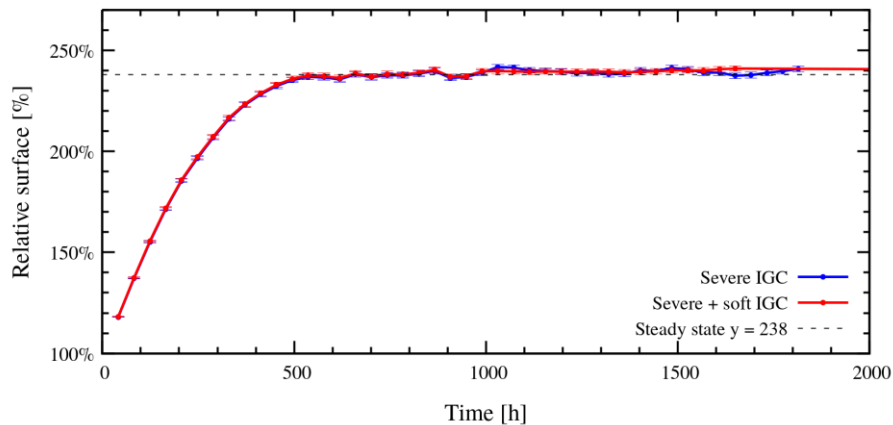
346 **Figure 10: Observation of the samples by Scanning Electron Microscope after the**
 347 **corrosion tests in the severe ($t_{\text{severe}} = 2564$ h) (a), soft ($t_{\text{soft}} = 16815$ h) (b) and change**
 348 **from severe ($t_{\text{severe}} = 1935$ h) to soft ($t_{\text{soft}} = 16815$ h, i.e. $t_{\text{severe+soft}} = 17783$ h) conditions**
 349 **(c).**

350
 351 Moreover, we investigated how the grooves angles distributions affect the surface in
 352 contact with the corrosive solution. For this purpose, the relative surface was determined
 353 from the CA simulations as described in the appendix 1 and 2. Results are given in Figure
 354 11. In both severe and soft conditions, the relative surface increases from its initial “flat
 355 surface value” (100%) to reach a larger steady state value. The steady state value is higher
 356 ($238.4 \pm 0.4\%$, estimated in the interval $t_{\text{severe}} = 1568 - 1732$ h) for the severe conditions
 357 (therefore for the thinner grooves angle) than in soft conditions ($223.7 \pm 0.5\%$, estimated
 358 in the interval $t_{\text{soft}} = 17325 - 20625$ h). This is in agreement with the results of Gwinner *et*
 359 *al.* obtained with a model based on a 2D geometrical approach [35].

360



361



362

363 **Figure 11: Relative surface for sections of the lattice for the three IGC corrosion**
 364 **regimes (CA simulations). The bottom plot is a zoom of the top one at short times.**

365

366 We showed that in stationary conditions, the IGC characteristics depend on the oxidizing
 367 power of the corrosive medium. In more severe conditions, the SS is polarized at higher
 368 potential in the transpassive domain which has different consequences on the corrosion of
 369 the SS. Firstly, the dissolution of the SS is faster (V_{gm} is larger). This has to be related to
 370 the presence of a thicker oxide on the surface evidenced by XPS. Secondly, the
 371 intergranular corrosion is faster (V_{ign} is larger), which leads to a shorter transient time to
 372 reach the IGC steady state (in accordance with [35], where the transient time is shown to
 373 be inversely proportional to V_{ign}). Moreover, the global corrosion rate reached at steady
 374 state (which corresponds to V_{ign}^*) is larger. Thirdly, the ratio V_{ign}/V_{gm} is increased which
 375 has the consequence that the grooves angles are thinner. Finally, the total surface reached
 376 at steady state is larger.

377

378 As discussed in the introduction, it is of practical interest to investigate the influence of
379 changing the nature of the corrosive medium during the life duration. This is the objective
380 of the following part.

381

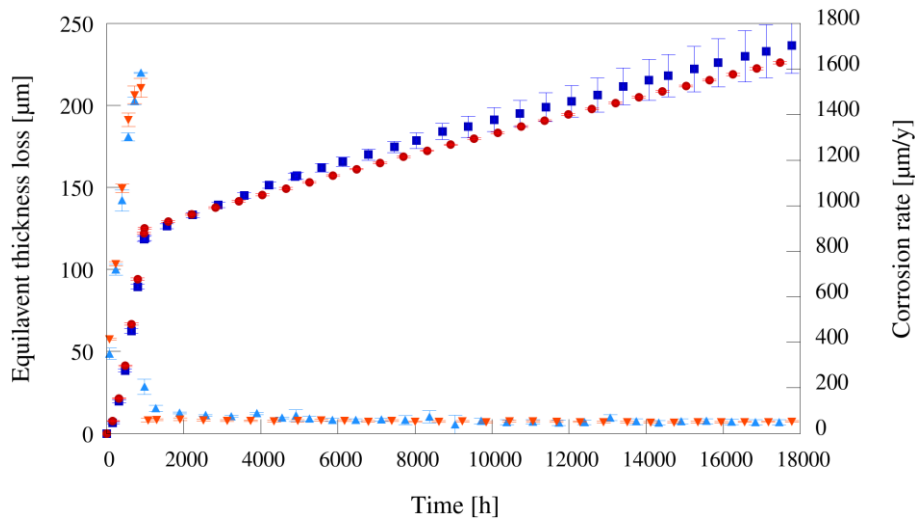
382 Change from severe to soft IGC conditions

383 In order to study the effect of a change in the IGC conditions, we firstly corroded samples
384 during 968 h in the conditions of severe IGC (with vanadium(V)) until the steady state is
385 reached. Figure 12 and Figure 13 display the evolution of the mass and the morphology as
386 a function of time, respectively. At the end of this early stage, the steady state is reached
387 in terms of mass loss (Figure 12) and surface morphology (Figure 13).

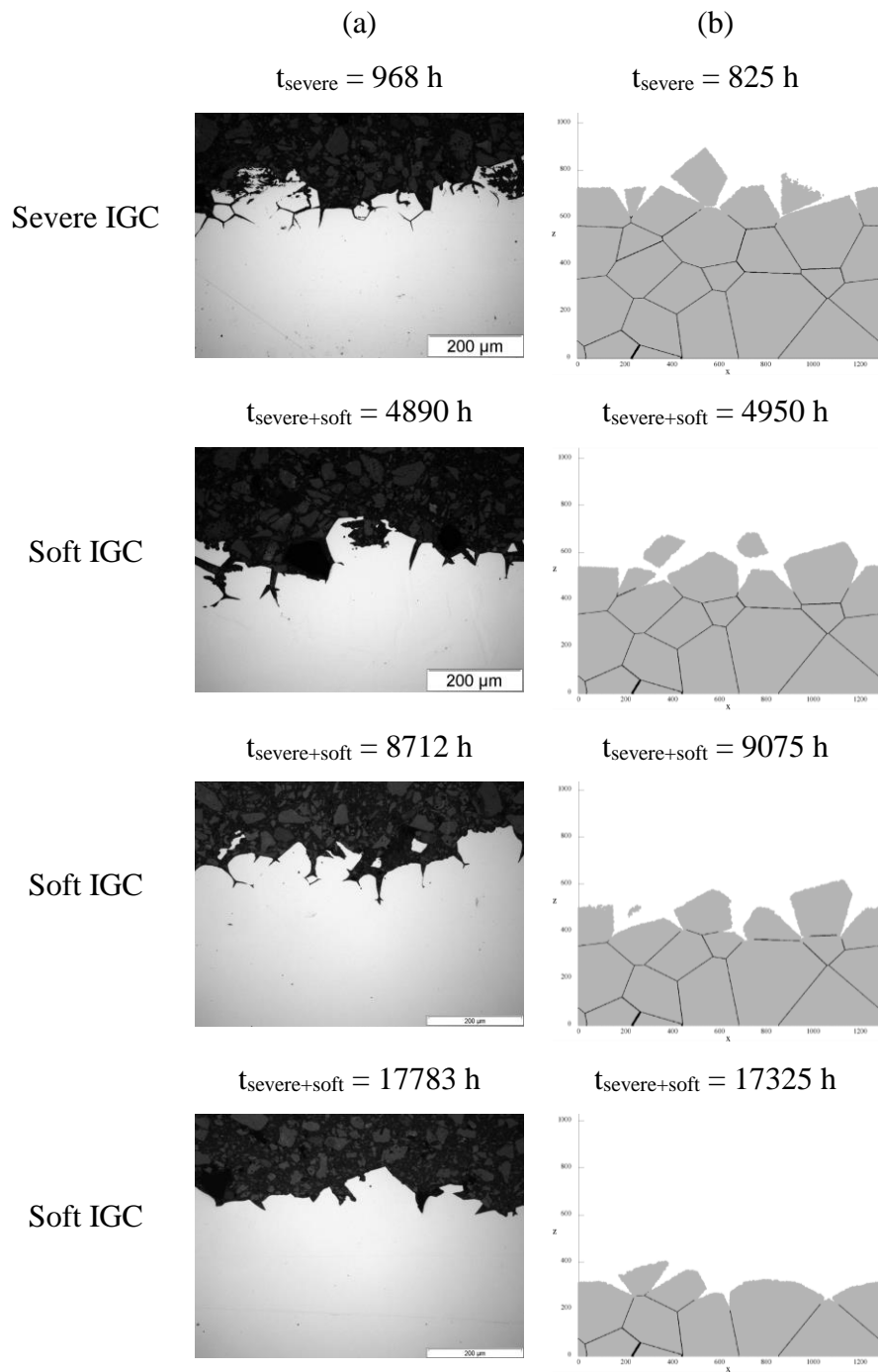
388 Then we changed the solution into soft conditions (without vanadium(V)). The evolution
389 of the corrosion rate is given in Figure 14 and is compared to the one in soft conditions
390 only. The corrosion rate suddenly decreases in accordance with the new soft IGC
391 conditions. However, it does not keep a constant value. It slowly decreases as a function
392 of time even if the solution (that means the corrosiveness) remains the same. The system
393 reaches a new steady state, which is identical to the previous soft IGC stationary case in
394 terms of corrosion rate (about $50 \mu\text{m}\cdot\text{y}^{-1}$). Moreover, the steady state is reached at the same
395 time in both cases. This transient time is in accordance with the one estimated by Equation
396 2. This corresponds to the time necessary to remove a thickness equivalent to the mean
397 grains size. Thus, whatever the history of the SS (already corroded in severe IGC
398 conditions or not), the corrosion needs to consume the equivalent of a layer of grains to
399 erase the effects of this history.

400 Figure 13 shows the evolution of the IGC morphology from the severe conditions at steady
401 state (at $t_{\text{severe}} = 968$ h) to the soft conditions (until $t_{\text{severe+soft}} = 17783$ h). A slow evolution
402 is observed between a highly rough surface (resulting from the severe IGC conditions) to
403 a less rough surface (resulting from the soft IGC conditions). In the same way, SEM
404 observations in Figure 10 show that the soft conditions tend to smooth the serious
405 intragranular corrosion induced by severe conditions. CA simulations were performed to
406 investigate quantitatively this point. The same input corrosion probabilities were
407 considered as for the previous simulations (Table 5). The first step was first modeled in
408 severe conditions during 990 h. Then the probabilities were changed into soft conditions
409 to model the rest of the simulation.

410 Simulations reproduce correctly the mass loss kinetics (Figure 12) and the evolution of the
411 morphology (Figure 13) observed experimentally. Figure 15 shows that the characteristics
412 of the grooves angles evolve from relatively thin angles under severe conditions to larger
413 angles in soft conditions. Consequently, the relative surface in contact with the solution
414 decreases slowly from a value of $238.7 \pm 0.7\%$ (estimated in the interval $t_{\text{severe}} = 1568 -$
415 1733 h) in severe conditions to about $225.4 \pm 0.5\%$ (estimated in the interval $t_{\text{severe+soft}} =$
416 $17325 - 20625$ h) in soft conditions, the same value as the experiment in steady soft
417 conditions.
418

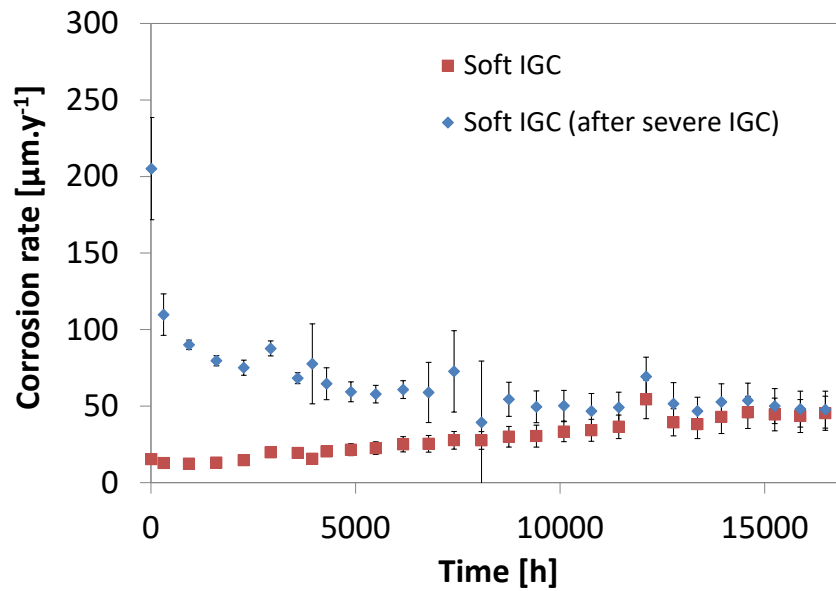


419
420 **Figure 12: Comparison between experimental results (in blue) and CA simulations**
421 **(in red) in the case of alternation a severe and a soft IGC. Squares represent the**
422 **equivalent thickness loss and triangles the corrosion rate.**
423



424 **Figure 13: Evolution of the IGC observed on cross-sections in the case of alternation**
 425 **a severe and a soft IGC. (a) experiment and (b) CA simulations.**

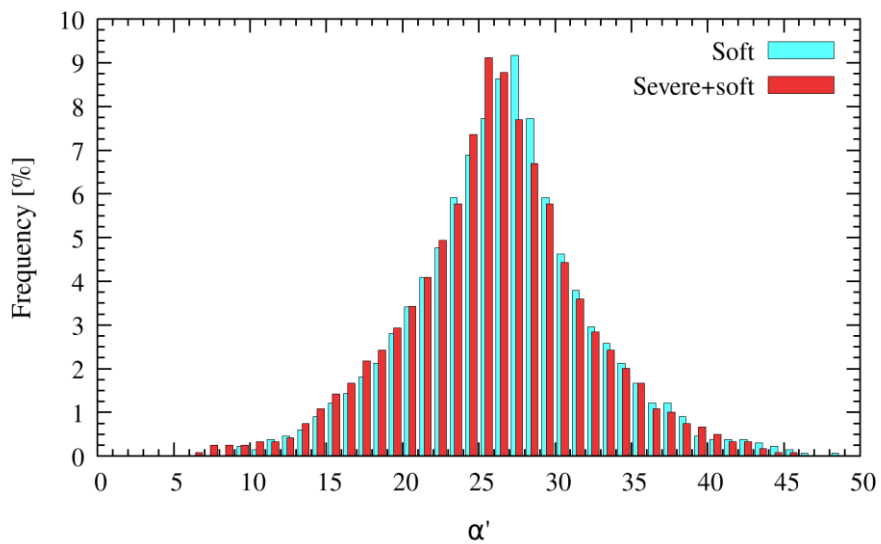
426



427

428 **Figure 14: Comparison of the corrosion rate estimated for soft IGC only and soft IGC**
 429 **after severe IGC (experimental results).**

430



431

432 **Figure 15: Distribution of the grooves angles α' in the steady state in soft (in blue,**
 433 **evaluated at $t_{\text{soft}} = 20625$ h) and in change from severe to soft (in red, evaluated at**
 434 **$t_{\text{severe+soft}} = 20625$ h) conditions (CA simulations). In both cases, histograms are**
 435 **realized with the same classes but are slightly shifted for a better view.**

436 The characteristics of the oxide layer on the surface also re-adapts to the new soft
 437 conditions (Figure 8). In particular, the apparent oxide thickness is similar in soft
 438 conditions and in change from severe to soft conditions (Figure 8 (a)).

439 Because of the oxide and morphology re-adaptation to the new soft conditions, the aspect
440 of the surface also changes from dark grey (characteristic of the severe conditions) to light
441 grey (characteristic of the soft conditions) as shown in Figure 7.

442

443

444

Conclusions

445 We first investigated the impact of the oxidizing character of the nitric medium on the
446 evolution of the IGC of an austenitic SS. In two different stationary chemical conditions
447 (severe and soft, respectively), we showed that the SS reaches a different steady state in
448 terms of the oxide and the geometrical natures of the interface: the oxide is thicker, the
449 intergranular grooves are thinner and the surface area is larger with the oxidizing character
450 of the nitric medium. Then we investigated the effect of an alternative “severe then soft”
451 corrosion sequence. We showed that the system re-adapted to the soft conditions after a
452 certain duration (which corresponds to the time necessary to corrode a thickness equivalent
453 to the mean grains size of the SS) without memory effect from the previous severe ones:
454 the corrosion rate, the geometrical nature of the interface and the thickness of the oxide
455 become similar to the system corroded in soft conditions only. In other words, whatever
456 the IGC history of a SS, the new conditions of IGC corrosion need to consume the
457 equivalent of a layer of grains to erase the effects of this history.

458

459

Acknowledgments

460

461 The authors thank Orano for financial support. They thank also R. Golchha for his
462 careful proofreading. D. di Caprio would like to thank Dr. B. Diawara for fruitful
463 discussions and introducing him to the marching cubes algorithm.

464

465

Appendix

466

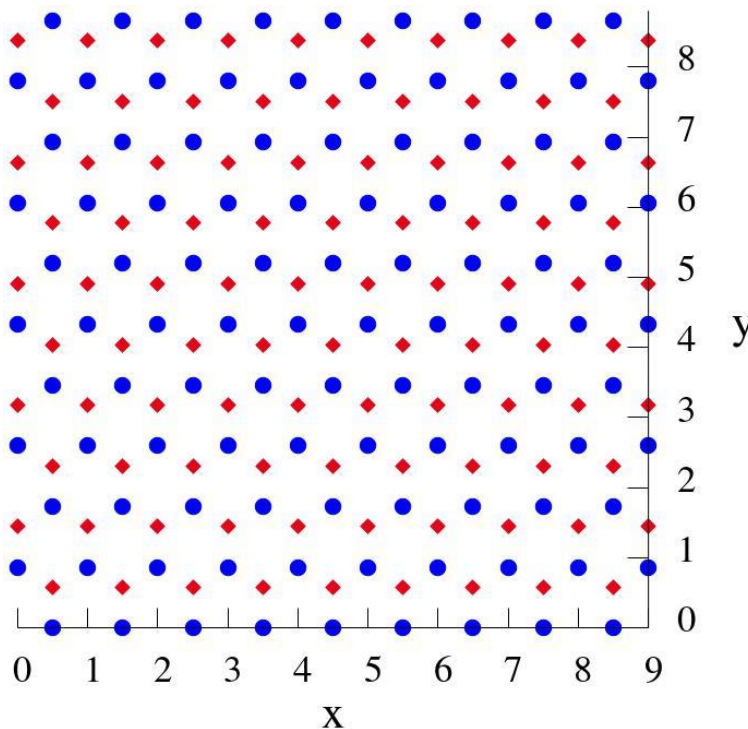
Appendix 1: solid/solution frontier estimation, marching square type algorithm

468 In this section, we detail the algorithm used to measure the length of the border line
469 between the solution cells and the solid corresponding to GRN or IGN cells. For 3D objects,
470 the marching cubes algorithm [48] is often used to determine contour lines. Given its
471 simplicity, the algorithm finds applications in video games but also in medicine, for 3D
472 visualization of volume data from magnetic resonance imaging and computed tomography
473 scans [48, 49]. In the case of 2D images, the algorithm is referred to as marching squares.
474 In the context of this paper, the algorithm is further adapted for a 2D grid based on
475 rectangles paving the plane instead of squares. The details about the system coordinates
476 used for the hexagonal lattice are given hereafter.

477

The hexagonal lattice

479 The plane of the hexagonal lattice structure is the horizontal Oxy plane, with, for $z = 0$, the
480 first line $y = 0$, points starting at $x = 0.5$ and placed in the Ox direction at a distance of 1 as
481 shown in Figure 16 in blue points.

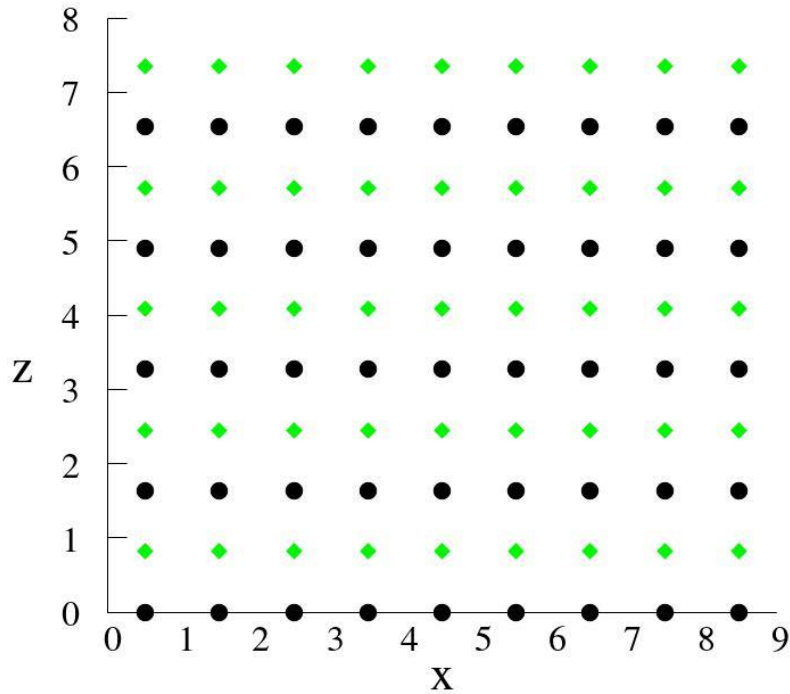


482

483 **Figure 16: Horizontal sections of the hexagonal lattice. Two consecutive planes, $z = 0$**
484 **and $z = (2/3)^{1/2}$, are shown with respectively blue and red points.**

485 Once these first two planes are defined, the rest of the lattice is derived. In particular, in
486 the experiments and in the simulations vertical sections are studied. The layout of points in
487 the vertical sections for the simulation is shown in Figure 17 where we have considered
488 vertical Oxz planes with constant y coordinate.

489



490

491 **Figure 17: Vertical sections of the lattice. Two consecutive planes for $y = 0$ and $y =$**
492 **$(3)^{1/2}/2$ are shown with respectively black and green points.**

493

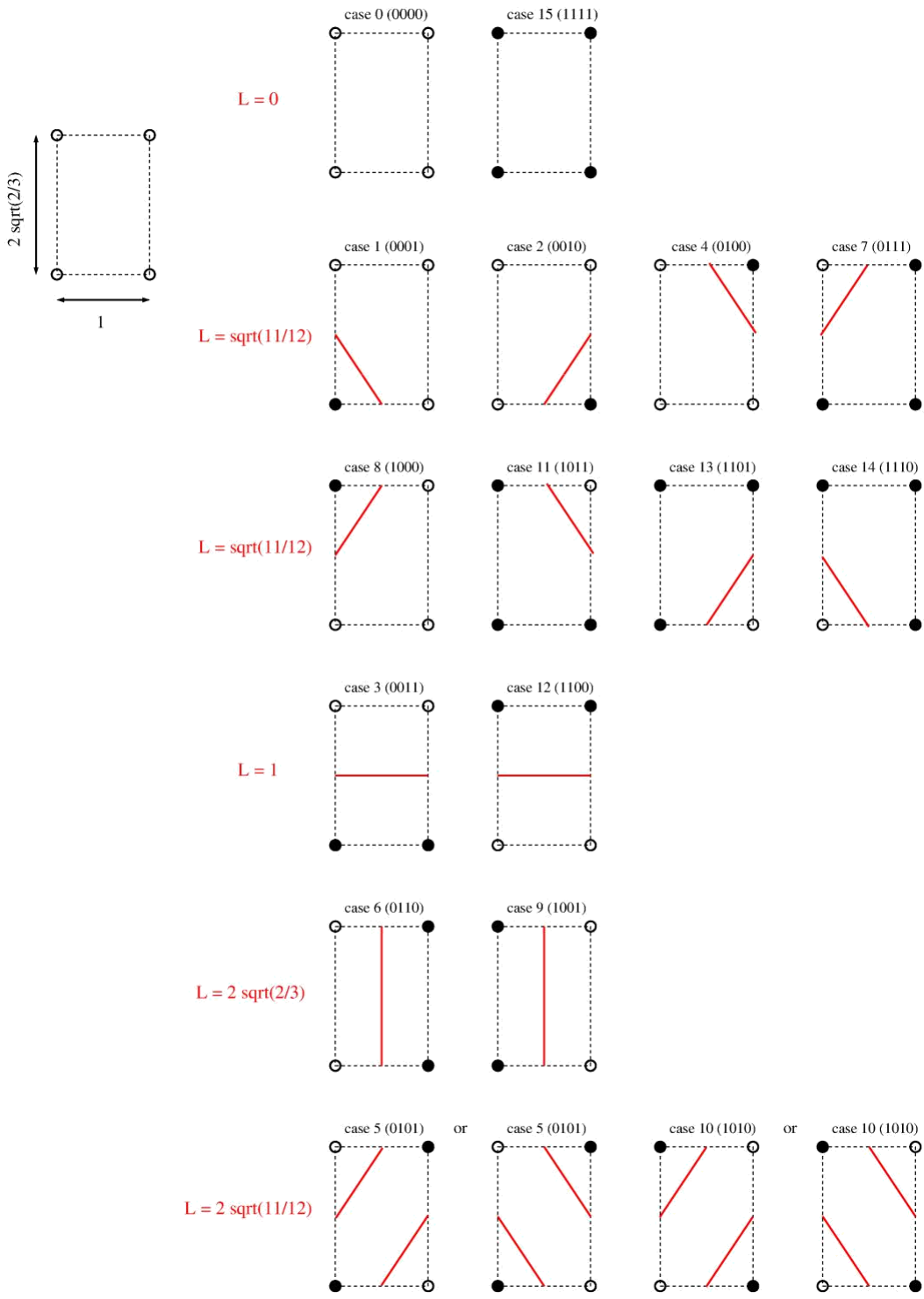
494 From the figure, it is clear that we have rectangles paving the plane.

495

496 *The marching rectangles algorithm*

497 Then, the algorithm consists in summing the contributions to the solution/solid border
498 coming from each rectangle in the plane. For this aim, we first list all possible contributions
499 coming from the configurations as shown in Figure 18. By assigning “1” to an intergranular
500 or granular point and “0” to a solution point and starting from the bottom left corner, in an
501 anticlockwise order, we obtain a binary number which is assigned to the corresponding
502 case.

503



504

505 **Figure 18: On the top left the elementary rectangle and its dimensions. On the right**
 506 **are listed the length contributions and the corresponding layout of the points. Empty**
 507 **circles are for solution points and black points are for solid granular or intergranular**
 508 **cells.**

509

510 The cases in the first line correspond to cases inside the solution or inside the solid and
 511 they naturally do not contribute to the border length: $L = 0$. The cases in the last line

512 correspond to a saddle point situation where we have two lines but for which the line
513 orientation can be ambiguous. However, the contribution to the border length is the same
514 for both orientations so that the result is unchanged despite the ambiguity. Other border
515 lengths correspond to their geometrical contribution. All rectangles constituting the lattice
516 are computed and their contribution is summed up which gives the final estimation of the
517 border length. The ratio of this length divided by the straight lateral length of the system is
518 what we consider to be the relative surface, which is in fact a line for the 2D sections.

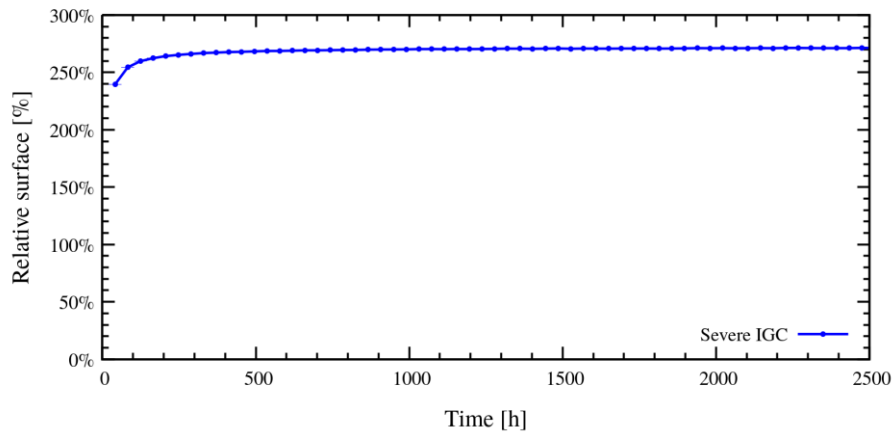
519

520 Appendix 2: extracting the grain scale relative surface

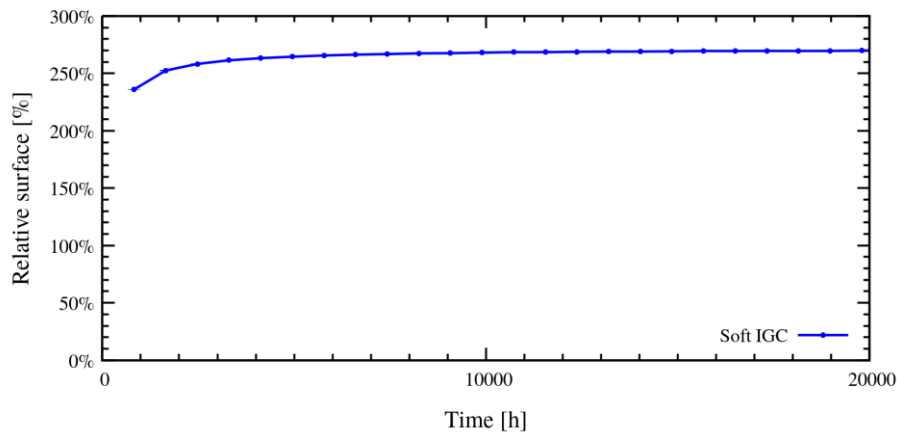
521 Simulated sections of the system in Figure 3, Figure 5 and Figure 13 clearly show that we
522 have two types of relative surface contributions. One with short length scale variations
523 corresponding to the dissolution of a single grain and one at a larger scale, the scale of
524 grains, due to IGC and detachment of grains. It is this last contribution that we are interested
525 in. However, the algorithm presented above does not distinguish the two, as it provides the
526 total separation line between solid and solution.

527 We present, hereafter, the method used to separate the contribution from IGC and grain
528 detachment from the contribution at a short length scale due to dissolution. For this aim,
529 we perform supplementary simulations for the dissolution of an exclusively granular
530 material with an initial plane surface and in the identical conditions of severe, soft and
531 variable IGC conditions as for the IGC material model. Results are obtained averaging over
532 2000 sections. Figure 19 shows the relative surface, roughness for the three cases.

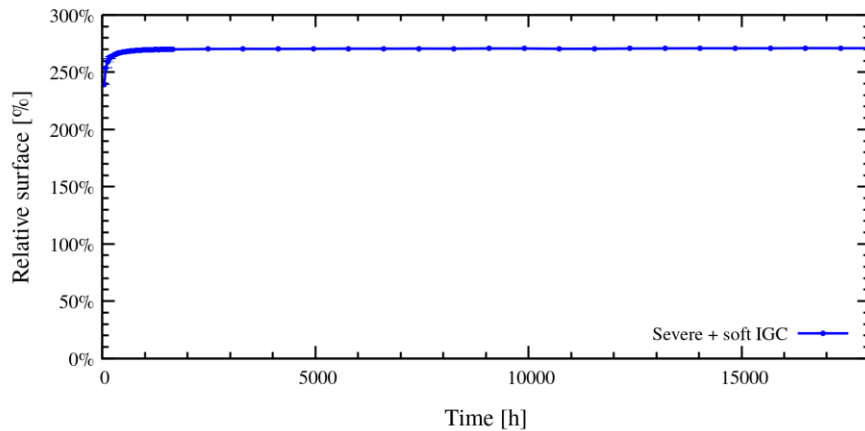
533



534



535



536

537 **Figure 19: Solid/solution relative interface for successively the severe, soft and**
 538 **variable IGC conditions for granular dissolution.**

539

540 The relative surface varies with time: it increases before reaching a steady state. This is
 541 why we use this time dependent quantity to renormalize the relative surface and not the
 542 steady state value. Thus the relative surface corresponding to IGC and grain detachment is
 543 obtained from the relative surface obtained by the algorithm by dividing it by the relative
 544 surface for exclusively granular dissolution. The procedure has been tested by applying it

545 to the study presented in [23], and the results compare well within the error bars. The results
546 in the case of the present paper study are presented in Figure 11. Averages are performed
547 using 100 Voronoï structures with for each 9 sections, this ensures that sections are
548 sufficiently spaced to avoid undesirable correlations.

549

550

References

551

- 552 1. Bal, K.S., J.D. Majumdar, and A.R. Choudhury, *Study of intergranular corrosion*
553 *mechanism of fiber laser welded 3-mm-thick Hastelloy C-276 sheet*. Corrosion
554 Science, 2019. **157**: p. 406-419.
- 555 2. Kaithwas, C.K., et al., *'Hall-Petch' type of relationship between the extent of*
556 *intergranular corrosion and grain size in a Ni-based superalloy*. Corrosion Science,
557 2020. **175**.
- 558 3. Zhang, J.Y., et al., *New perspectives on the grain boundary misorientation angle*
559 *dependent intergranular corrosion of polycrystalline nickel-based 625 alloy*.
560 Corrosion Science, 2020. **172**.
- 561 4. de Bonfils-Lahovary, M.L., et al., *Influence of hydrogen on the propagation of*
562 *intergranular corrosion defects in 2024 aluminium alloy*. Corrosion Science, 2019.
563 **148**: p. 198-205.
- 564 5. Kairy, S.K., et al., *The role of microstructure and microchemistry on intergranular*
565 *corrosion of aluminium alloy AA7085-T7452*. Corrosion Science, 2018. **143**: p.
566 414-427.
- 567 6. Zhang, X.X., et al., *Intergranular corrosion in AA2024-T3 aluminium alloy: The*
568 *influence of stored energy and prediction*. Corrosion Science, 2019. **155**: p. 1-12.
- 569 7. Hu, S., et al., *Intergranular corrosion behavior of low-chromium ferritic stainless*
570 *steel without Cr-carbide precipitation after aging*. Corrosion Science, 2020. **166**.
- 571 8. Morshed-Behbahani, K., et al., *An electrochemical study on the effect of*
572 *stabilization and sensitization heat treatments on the intergranular corrosion*
573 *behaviour of AISI 321H austenitic stainless steel*. Corrosion Science, 2018. **138**: p.
574 28-41.
- 575 9. Pradhan, S.K., P. Bhuyan, and S. Mandal, *Individual and synergistic influences of*
576 *microstructural features on intergranular corrosion behavior in extra-low carbon*
577 *type 304L austenitic stainless steel*. Corrosion Science, 2018. **139**: p. 319-332.
- 578 10. Fauvet, P., *Corrosion issues in nuclear fuel reprocessing plants*, in *Nuclear*
579 *corrosion science and engineering*, D. Feron, Editor. 2012, Woodhead Publishing.
580 p. 679-728.
- 581 11. Fauvet, P., et al., *Corrosion mechanisms of austenitic stainless steels in nitric media*
582 *used in reprocessing plants*. Journal of Nuclear Materials, 2008. **375**(1): p. 52.
- 583 12. Kato, C., *Corrosion in Nuclear Fuel Reprocessing Plants: Corrosion in Boiling*
584 *Nitric Acid*, in *Comprehensive Nuclear Material book*. 2020, Elsevier.
- 585 13. Emery, A., *Corrosion intergranulaire des aciers inoxydables austénitiques en*
586 *milieu acide nitrique oxydant*. 2019, Université PSL.
- 587 14. Komatsu, A., et al., *Effect of local segregation of phosphorous on intergranular*
588 *corrosion of type 310 stainless steel in boiling nitric acid*. Zairyo to Kankyo, 2014.
589 **63**(3): p. 98-103.

- 590 15. Tcharkhtchi-Gillard, E., et al., *Kinetics of the oxidation of stainless steel in hot and*
591 *concentrated nitric acid in the passive and transpassive domains.* Corrosion
592 Science, 2016. **107**: p. 182-192.
- 593 16. Ueno, F., et al. *Intergranular corrosion mechanism of ultra-low carbon type 304*
594 *stainless steel in a nuclear reprocessing plant.* in *Global 2007.* 2007. Boise, Idaho.
- 595 17. Ueno, F., et al., *Corrosion phenomenon of stainless steel in boiling nitric acid*
596 *solution using large-scale mock-up of reduced pressurized evaporator.* Journal of
597 Nuclear Science and Technology, 2008. **45**(10): p. 1091-1097.
- 598 18. Ueno, F., et al. *Study on the effect of phosphorous concentration on intergranular*
599 *corrosion of stainless steel in boiling nitric acid solution.* in *Eurocorr.* 2014. Pise
600 (Italie).
- 601 19. Whillock, G.O.H. and B.F. Dunnett. *Intergranular corrosion testing of austenitic*
602 *stainless steels in nitric acid solutions.* in *Eurocorr 2004.* 2004. Nice (France):
603 Société de Chimie Industrielle, Paris (France). INIS-FR-3830.
- 604 20. Whillock, G.O.H., B.F. Dunnett, and M. Takeuchi, *Techniques for measuring the*
605 *end-grain corrosion resistance of austenitic stainless steels.* Corrosion, 2005.
606 **61**(1): p. 58-67.
- 607 21. Bague, V., et al., *Determination of the long-term intergranular corrosion rate of*
608 *stainless steel in concentrated nitric acid.* Journal of Nuclear Materials, 2009.
609 **392**(3): p. 396-404.
- 610 22. Jothilakshmi, N., P.P. Nanekar, and V. Kain, *Assessment of Intergranular*
611 *Corrosion Attack in Austenitic Stainless Steel Using Ultrasonic Measurements.*
612 Corrosion, 2013. **69**(4): p. 388-395.
- 613 23. Guiso, S., et al., *Intergranular corrosion: Comparison between experiments and*
614 *cellular automata.* Corrosion Science, 2020. **177**: p. 108953.
- 615 24. Gwinner, B., et al., *A stereological approach for measuring the groove angles of*
616 *intergranular corrosion.* Corrosion Science, 2017. **115**: p. 1-7.
- 617 25. Ioka, I., et al. *Susceptibility of intergranular corrosion for extra high purity*
618 *austenitic stainless steel in nitric acid.* in *Proceedings of 16th International*
619 *Conference on Nuclear Engineering, ICONE-16.* 2008.
- 620 26. Motooka, T., C. Kato, and M. Yamamoto, *Effect of Reoxidation Rate of Chromium*
621 *and Vanadium Ions on Corrosion Rate of Stainless Steel in Boiling Nitric Acid*
622 *Solutions.* Corrosion Engineering, 2010. **59**(1): p. 12-20.
- 623 27. Motooka, T. and M. Yamamoto, *Corrosion behavior of stainless steel in nitric acid*
624 *solutions including neptunium.* Zairyo to Kankyo 2008. **57**(12): p. 536-541.
- 625 28. Ningshen, S., et al., *Corrosion assessment of nitric acid grade austenitic stainless*
626 *steels.* Corrosion Science, 2009. **51**(2): p. 322-329.
- 627 29. Takeuchi, M. and G.O.H. Whillock, *Effect of Endgrain Attack on Corrosion of*
628 *18Cr–10Ni Austenitic Stainless Steel*
629 *in Simulated Dissolver Liquor.* Journal of NUCLEAR SCIENCE and TECHNOLOGY,
630 2004. **41**(6): p. 702-708.
- 631 30. Wang, W., et al., *Influence of grain size on susceptibility of Cr-Ni austenitic*
632 *stainless steel to intergranular attack in nitric acid.* Journal of Iron and Steel
633 Research, 2010. **22**(1).
- 634 31. Ioka, I., et al., *Correlation between intergranular corrosion and impurities of extra*
635 *high purity austenitic stainless steels.* Journal of Power and Energy Systems, 2010.
636 **4**(1): p. 105-112.
- 637 32. Guiso, S., et al., *Intergranular corrosion: Comparison between experiments and*
638 *cellular automata.* Corrosion Science, 2020. **177**.

- 639 33. Ningshen, S. and M. Sakairi, *Corrosion degradation of AISI type 304L stainless*
640 *steel for application in nuclear reprocessing plant.* Journal of Solid State
641 Electrochemistry, 2015. **19**(12): p. 3533-3542.
- 642 34. Robin, R., F. Miserque, and V. Spagnol, *Correlation between composition of*
643 *passive layer and corrosion behavior of high Si-containing austenitic stainless*
644 *steels in nitric acid.* Journal of Nuclear Materials, 2008. **375**(1): p. 65-71.
- 645 35. Gwinner, B., et al., *Towards a reliable determination of the intergranular corrosion*
646 *rate of austenitic stainless steel in oxidizing media.* Corrosion Science, 2016. **107**:
647 p. 60-75.
- 648 36. Igarashi, T., et al. *Intergranular Corrosion Simulation of Stainless Steel*
649 *Considering Nitric Acid Solution Condition.* in Eurocorr. 2016.
- 650 37. Igarashi, T., et al. *Three dimensional computational modelling and simulation of*
651 *intergranular corrosion propagation of stainless steel.* in *19th International*
652 *Corrosion Congress.* 2014. Jeju, Korea.
- 653 38. Guiso, S., et al., *Influence of the grid cell geometry on 3D cellular automata*
654 *behavior in intergranular corrosion.* Journal of Computational Science, 2021. **53**:
655 p. 101322.
- 656 39. Bhise, S. and V. Kain, *Methodology based on potential measurement for predicting*
657 *corrosion behaviour of SS 304L in boiling nitric acid containing oxidising ions.*
658 Corrosion Engineering, Science and Technology, 2012. **47**(1).
- 659 40. Ghiban, B., et al., *Austenitic stainless steels corrosion properties modified by*
660 *silicon alloying.* Metalurgia International, 2008. **13**(7): p. 39-42.
- 661 41. Kain, V., et al., *Corrosion of non-sensitized austenitic stainless steels in nitric acid*
662 *environment: an electrochemical approach.* Advanced Materials Research
663 (Durnten-Zurich, Switzerland), 2013. **794**: p. 517-529.
- 664 42. Pourbaix, M., *Atlas d'équilibres électrochimiques à 25°C.* 1963, Paris: Gauthier-
665 Villars & Cie.
- 666 43. Grosvenor, A.P., et al., *Investigation of multiplet splitting of Fe 2p XPS spectra and*
667 *bonding in iron compounds.* SURFACE AND INTERFACE ANALYSIS, 2004.
668 **36**(12): p. 1564-1574.
- 669 44. Marchetti, L., et al., *XPS study of Ni-base alloys oxide films formed in primary*
670 *conditions of pressurized water reactor.* SURFACE AND INTERFACE
671 ANALYSIS, 2015. **47**(5): p. 632-642.
- 672 45. Laurent, B., et al., *Dissolution and Passivation of a Silicon-Rich Austenitic*
673 *Stainless Steel during Active-Passive Cycles in Sulfuric and Nitric Acid.* Journal of
674 The Electrochemical Society, 2017. **164**(13): p. C892-C900.
- 675 46. Beaunier, L., *Corrosion of grain boundaries : initiation processes and testing.*
676 Journal de Physique, 1982. **Colloque C6, supplement to Journal de Physique n°**
677 **12**(Tome 43): p. C6-271 – C6-282.
- 678 47. Beaunier, L., M. Froment, and C. Vignaud, *A kinetical model for the*
679 *electrochemical grooving of grain boundaries.* Electrochimica Acta, 1980. **25**(10):
680 p. 1239-1246.
- 681 48. Lorensen, W.E. and H.E. Cline, *Marching cubes: a high resolution 3D surface*
682 *construction algorithm,* in *Seminal graphics: pioneering efforts that shaped the*
683 *field.* 1998, Association for Computing Machinery. p. 347–353.
- 684 49. Zhang, Y.J., *Geometric Modeling and Mesh Generation from Scanned Images.*
685 2018, Chapman and Hall/CRC. p. 145-149.